

# PROCEEDINGS OF SPIE

[SPIDigitalLibrary.org/conference-proceedings-of-spie](https://spiedigitallibrary.org/conference-proceedings-of-spie)

## Detector and control system design and performance for the SuMIRe prime focus spectrograph (PFS) cameras

Gunn, James, Fitzgerald, Roger, Hart, Murdock, Hope, Stephen, Loomis, Craig, et al.

James E. Gunn Sr., Roger Fitzgerald, Murdock Hart, Stephen C. Hope, Craig Loomis, Grant O. Peacock, Mirek Golebiowski, Michael A. Carr, Stephen A. Smee, Naoyuki Tamura, Naruhisa Takato, Atsushi Shimono, "Detector and control system design and performance for the SuMIRe prime focus spectrograph (PFS) cameras," Proc. SPIE 9908, Ground-based and Airborne Instrumentation for Astronomy VI, 990893 (9 August 2016); doi: 10.1117/12.2233400

**SPIE.**

Event: SPIE Astronomical Telescopes + Instrumentation, 2016, Edinburgh, United Kingdom

# Detectors and detector control system design and performance for the SuMIRe Prime Focus Spectrograph (PFS) cameras

James E. Gunn<sup>a</sup>, Roger Fitzgerald<sup>e</sup>, Murdock Hart<sup>b</sup>, Stephen C. Hope<sup>b</sup>, Craig Loomis<sup>a</sup>, Grant O. Peacock<sup>b</sup>, Mirek Golebiowski<sup>b</sup>, Michael A Carr<sup>a</sup>, Stephen A Smee<sup>b</sup>, Naoyuki Tamura<sup>c</sup>, Naruhisa Takato<sup>d</sup>, and Atsushi Shimono<sup>c</sup>

<sup>a</sup>Princeton University, Department of Astrophysical Sciences, Princeton, NJ 08544, USA

<sup>b</sup>Johns Hopkins University, Department of Physics and Astronomy, 3701 San Martin Drive, Baltimore, MD 21218, USA

<sup>c</sup>Kavli Institute for the Physics and Mathematics of the Universe (WPI), The University of Tokyo, 5-1-5, Kashiwanoha, Kashiwa 277-8583, Japan

<sup>d</sup>Subaru Telescope, National Astronomical Observatory of Japan, 650 North A'ohoku Pl. Hilo, HI 96720, USA

<sup>e</sup>Fitzgerald Engineering, PO Box 462, Berlin, MD 21811, USA

## ABSTRACT

We discuss the design, construction, and performance of the detector system for the SuMIRe Prime Focus Spectrograph (PFS). SuMIRe PFS is a massively multi-plexed ground-based spectrograph consisting of four identical spectrograph modules, each receiving roughly 600 fibers from a 2394 fiber robotic positioner at the prime focus. Each spectrograph module has three channels covering the wavelength ranges 3800Å-6400Å, 6400-9550Å. and 9550-12600Å, with the dispersed light being imaged in each channel by a f/1.07 vacuum Schmidt camera. In this paper we describe the CCD system for the two visible channels and the overall control and data acquisition systems for the cameras, and discuss the test system for detector characterization. This system will also serve for testing the H4RG infrared detectors for the near IR channel. The first red system, utilizing a 200-micron thick fully depleted p-channel Hamamatsu CCD, is finished and has been tested. The performance is excellent, with low noise, high CTE, and very good low-level and overall linearity. The test system uses essentially all the 'flight' electronics and power supplies, in an effort to assess performance in an environment as nearly like the one to be seen in operation as possible.

**Keywords:** Cryostat, Spectrograph, Camera, CCD, Cryocooler, IR detector

## 1. INTRODUCTION

The SuMIRe (Subaru Measurement of Images and Redshifts) umbrella project for the Subaru Telescope consists of the HyperSuprimeCam 104-CCD imager (HSC),<sup>1</sup> now in regular operation, the Subaru Prime Focus Spectrograph (PFS),<sup>2</sup> a 2394-fiber low-dispersion spectrograph now under construction, and the long-term astronomical surveys to be carried out with these instruments.<sup>3</sup> The HSC imaging survey is now in its second year of operation.

This paper describes the detector system for PFS. The fibers from the Prime Focus Instrument (PFI) run from the Cobra<sup>4</sup> fiber positioners through a fiber cable system<sup>5</sup> to a set of MTP connectors which connect the removable PFI to a long fiber cable fixed to the telescope and then to another set of MTP connectors on the bodies of the spectrographs, which will reside on the IR4 floor of the Subaru Dome. There are 4 spectrographs,<sup>6</sup> each accommodating about 600 fibers, which run from the connectors to a fiber slit. The slit illuminates a common collimator and three cameras/gratings via two dichroics. The dispersion elements are VPH gratings; the beam size is 275mm.

---

Further author information: (Send correspondence to James E. Gunn)  
E-mail: jeg@astro.princeton.edu, Telephone: 1 609 258 3802

The wavelength ranges for the three arms of the spectrographs are 3800-6400Å, 6400-9550Å, and 9550-12600 Å with some overlap, and are covered simultaneously, so that the spectrograph yields spectra from 3800Å to 1.26 microns with no gaps. The central resolving powers in the three arms is about 2400 in the blue arm, 2900 in the red arm, and 4300 in the NIR arm; the wavelength resolution is roughly constant at about 3Å throughout the spectrum.

There is another mode in which a higher angular dispersion disperser assembly incorporating a high-index grism can be substituted for the red grating, yielding a resolving power of about 5000 in the center of the red band.

Negative microlenses on the fiber entrances slow the f/2.2 primary f/ratio to f/2.8 to facilitate transmission by the fibers. The fiber cores are 128 microns in diameter, which corresponds to an average angle of 1.1 arcseconds on the sky at the entrances to the microlenses.

The cameras are vacuum Schmidts<sup>7</sup> with two-element aspheric correctors and an active f/ratio of 1.07, resulting in a demagnification slit-to-detector of about 1/2.5; the fibers make an image about 49 microns in diameter on the detectors, and the optics are sufficiently good that this diameter is the FWHM and 50% EE diameter on the detectors.

This paper describes the detector systems for these spectrographs. In the blue arm of each is a two-element mosaic consisting of a pair of fully depleted p-type Hamamatsu S10892-1628(X) 4192 x 2048 15-micron pixel devices on 100-micron thick high-resistivity silicon with a custom multilayer coating optimized in the blue. The design QE as furnished by Hamamatsu is shown in Figure 1.

The red detectors are similar; a pair of Hamamatsu S10892-1629(X) CCDs with the same geometry and mask set as the blue ones, but built on 200-micron thick silicon, and with a coating optimized in the red (Figure 2). These detectors are essentially identical to those used in the HyperSuprimeCam. We use the detectors only out to 9550Å, but the tradeoff of QE with operating temperature and hence dark current is still fairly serious, and will be optimized.

In the NIR arm, Teledyne H4RG-15 4K x 4K detectors with 1.7-micron cutoff HgCdTe will be used, also with 15 micron pixels.

Since the geometry and pixel size of all the detectors are essentially the same, the optical systems and cryostats for all three can be and are essentially identical, though the mechanics are considerably different because of the necessity to cool the environment of the NIR detector to suppress the thermal background. The CCD cryostats are described in detail in Smee *et. al.*<sup>8</sup> in this volume, and a preliminary description of the IR cryostat in a 2014 SPIE paper.<sup>9</sup>

With 15 micron pixels, the fibers produce an image a bit more than 3 pixels in diameter. Even though the resolution is then more than 2 pixels, the PSF has very steep edges and the spectra will be undersampled as a

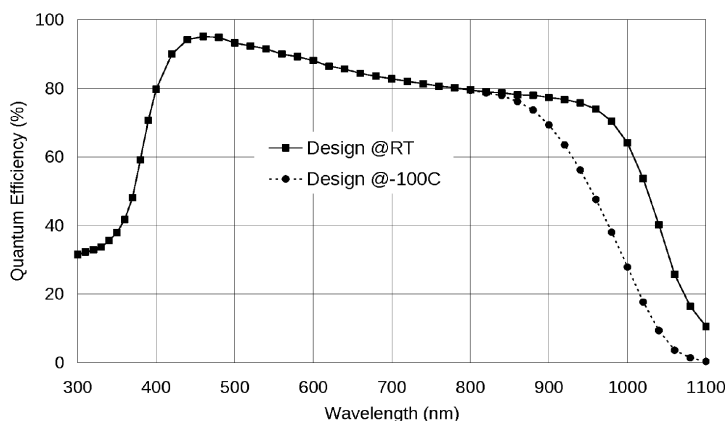


Figure 1. Design QE of blue Hamamatsu 2K x 4K CCD

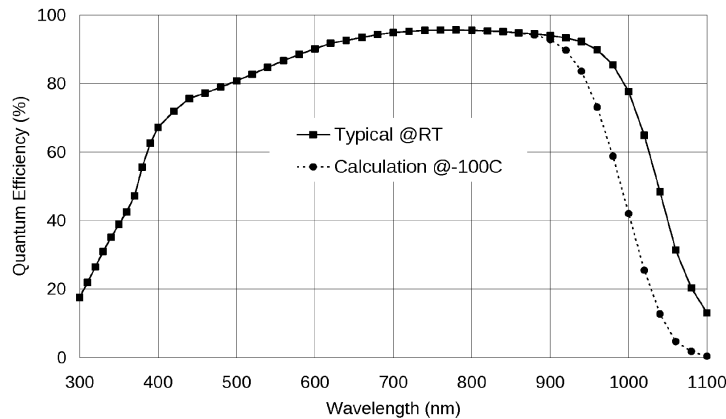


Figure 2. Design QE of red Hamamatsu 2K × 4K CCD

result by roughly a factor of two, which is a serious challenge to the reduction software development. This is especially acute because the targets for the survey with this instrument have surface brightnesses over the fiber diameter typically more than an order of magnitude below the sky continuum, and many orders of magnitude below the main bodies of the images of the bright OH lines, and it is necessary to subtract the sky from one fiber from sky+object in another fiber to very high accuracy.

## 2. THE CCD SYSTEM ELECTRONICS

The CCD electronics were discussed in the proceedings of the last SPIE astronomy conference<sup>10</sup> and have changed only slightly in the final version, so we will only review the system here briefly.

Each of the Hamamatsu CCDs has 4 2-phase serial registers, each addressing 512 columns of the 2048-column wide array. Each serial register has one amplifier with a gain of roughly  $4\mu\text{V}$  per electron. This output amplifier is a standard MOSFET follower buffered by an off-chip JFET follower mounted on the detector package. The noise of the combination is such that at 75kHz readout one should achieve about 3 electrons read noise using a conventional CDS sampling system.

The imaging array uses a 3-phase architecture with separate clock lines for the upper and lower halves, so the device can be used as in frame-store mode. There are 32 tapered pixels at the bottom of the array to feed the serials which are not used in imaging.

Since we use 2 detectors to make a 4K x 4K array, we have eight channels per camera. These signals are amplified by a preamp which is built around Analog Devices AD8610 JFET-input operational amplifiers, which have low noise ( $6\text{nV}/\sqrt{\text{Hz}}$ ) and reasonably high bandwidth (25MHz). These amplifiers are used throughout the analog signal chain, though the downstream ones are the double versions (8620). The preamp is capacitively coupled to the CCD output transistor through a DC restoration circuit which is reset during the serial transfer time for each pixel. The preamp is built on a small all-surface mount (except for the polypropylene coupling capacitors) board which is mounted behind the detector in its shadow. The preamps have a noninverting gain of 6. We want to run with a fullscale signal of about 85,000 electrons, which is an output signal from the CCD of about 0.35V, so the video signal from the preamp is about 2V.

The signal chain/ADC electronics is accommodated on a small circular board which is mounted in one of the vacuum ports on the cryostat, in turn mounted to the 'FEE' (Front End Electronics) board whose plated features form a vacuum seal for that port. This assembly is shown in Figure 3

The signal chain is a conventional analog CDS circuit with a differential input (the common video line for each channel is arranged to have the same output impedance as the active video line). This differential amplifier feeds an inverter and an integrator, all implemented with AD8620s. The overall gain of the signal chain following the preamp is 2.4. The integrator, which serves as a sample/hold as well, feeds a bipolar Analog Devices AD7690

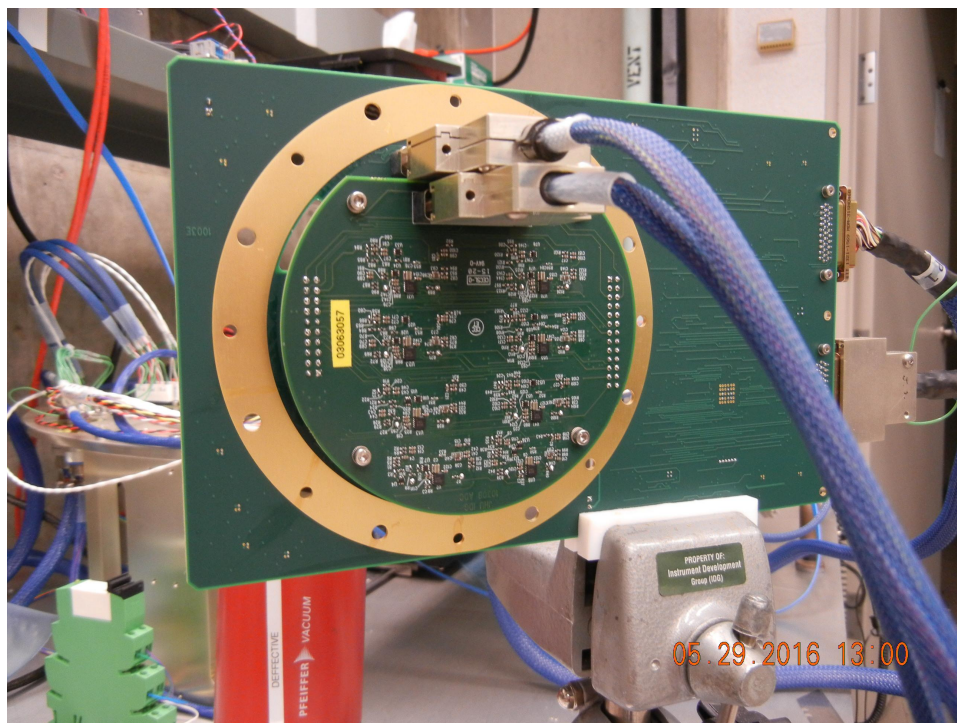


Figure 3. Photograph of the ADC-FEE board assembly from the vacuum side, showing the circular signal-chain/ADC board. The digital FEE circuitry is on the other side of the larger rectangular board. The plated, drilled ring, duplicated on the other side, makes an O-ring vacuum seal with the port on this side and an O-ring seal with a cap on the other.

18-bit ADC, used as a unipolar 0-5V device. This ADC can use a reference at the Vcc rail, which is fortunate, since the voltage noise in the signal chain is dominated by the ADC and appears to independent of the reference. We get 16-bit data by using the device in unipolar mode and dropping the LSB; the noise is about 0.6 of our LSB, which corresponds to about 0.8 electrons. There are DAC-generated reference voltages which control the integrator slopes both at reference time and at video time to minimize crossover noise for small signals. The ADCs have serial output and can be ganged to generate a long serial word. All four ADCs for a given CCD are so ganged, so the data system is fed a 72-bit word for each pixel at 50MHz. This transfer occurs during the serial CCD charge transfer time and has no impact on the overall timing nor on the noise performance.

The adjustable voltage levels for the many operating, clock rail, bias, and trim voltages for the CCDs are set by AD5360 16 channel, 16-bit serial-input DACs controlled by a PIC18F67K22 microcontroller on the FEE board. This board, as mentioned above, forms a vacuum seal; the relatively noisy digital circuitry is outside the vacuum sealing ring and the more sensitive analog circuitry in the vacuum.

The clocks are generated in a separate processor, the BEE ('back-end-electronics'), in the electronics enclosure on the back of the cryostat (the 'piepan'), as LVDS digital signals, and are transformed to clock signals swinging to the various CCD rail voltages and shaped by RC filters on the FEE board using CMOS analog switches, mostly ADG1434s.

The BEE comprises two commercial boards, a PC104 processor and an FPGA, respectively a CMX32MCS1200-2048 SBC with a ULV722 Celeron M processor and an RTD FPGA35S6045HR daughter board using a Xilinx Spartan-6. The FPGA generates all the CCD clock signals and receives and decodes the image data. The computer manages most of the housekeeping and interlocks, not only for the detector system, but also for the whole cryostat, including vacuum, temperature, power, focus, etc, in conjunction with a set of intelligent special-purpose cards. It also manages the image intermediate storage and transmission to the observatory computing system. The BEE system is described more fully in Steve Smee's paper in this volume in its control aspects.<sup>8</sup>

### 3. THE TEST CRYOSTATS

The detectors, both the CCDs and the IR detectors, are tested and qualified in one of a pair of test cryostats<sup>11</sup> using the same Sunpower Cryotel GT40 cryocooler as is used in the camera cryostats. The cryostats can be simply adapted to mount either the CCD focal-plane assembly or the H4RG focal-plane assembly. The two are mechanically essentially identical, though one of them is intended as an operational test unit; the other is primarily intended for metrology and reflectance measurements at operating temperature.

For the operational cryostat, ancillary light sources with a monochromator and a 12-inch integrating sphere can supply uniform monochromatic illumination over the full required wavelength range. The illumination is monitored by a calibrated photodiode at the integrating sphere and another calibrated photodiode can be incorporated in the cryostat at the focal plane for cross-calibration for the measurement of QE. A 10 millicurie Fe-55 source on a movable arm for CTE and diffusion measurements is incorporated and an external subpixel ( 5 micron) source to investigate pixel crosstalk, electrostatic effects ('brighter-fatter'), and persistence is nearing completion. An externally movable cold shutter is incorporated for dark current measurements for the IR devices

Since the CCD focal plane consists of two separate sensors and the cameras are very fast (f/1.07), it is necessary to mount the sensors on the aluminum nitride cold plate very carefully and shim them so as to present a flat focal surface to the camera. Since both the CCD packages and the cold plate are aluminum nitride, this setup should not change as operating temperature is reached, but this is checked. The flatness is measured using a coordinate measuring machine and a white-light confocal microscope, which has a working distance large enough to allow measuring the surface of the detectors through the test cryostat window. Thus the flatness can be measured at any temperature reachable by the focal plane assembly in the cryostat. We have been able to achieve about 2 microns RMS contribution from mounting error, and the flatness error is completely dominated by the nonflatness of the devices themselves, which are typically 10 microns P-V. The detector height is set with three invar washer shims under the three CCD mounting posts. The shims are cut from a square invar tube using wire EDM; their thickness is controlled to better than one micron. It generally takes only one to two iterations to achieve satisfactory flatness. The situation for both the first red CCD and the first blue one are shown in Figures 4 and 5.

The test cryostat is shown in Figure 6 on the CMM table with the confocal microscope as used to measure detector flatness.

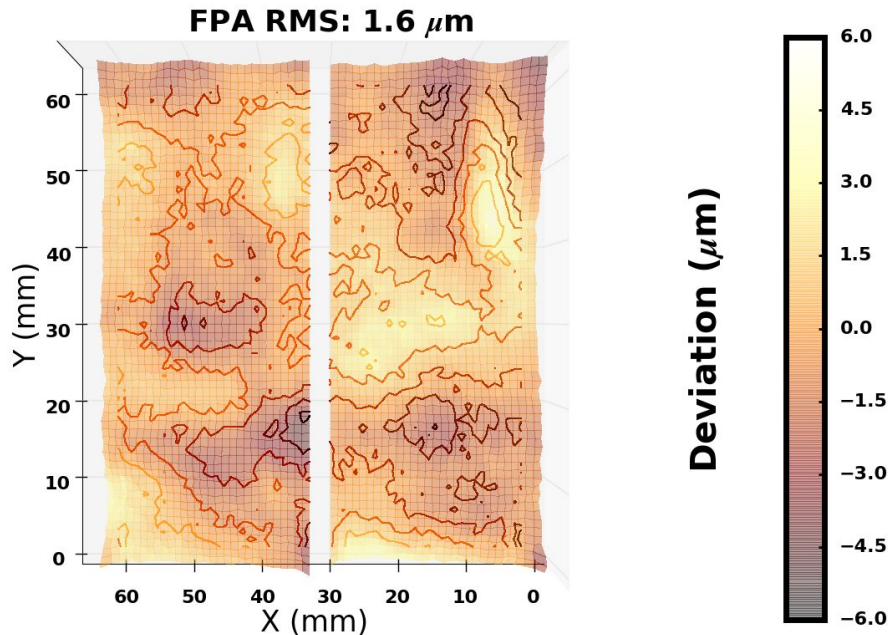


Figure 4. Contour map of the red detector pair at -100C; the changes from room temperature are negligible.

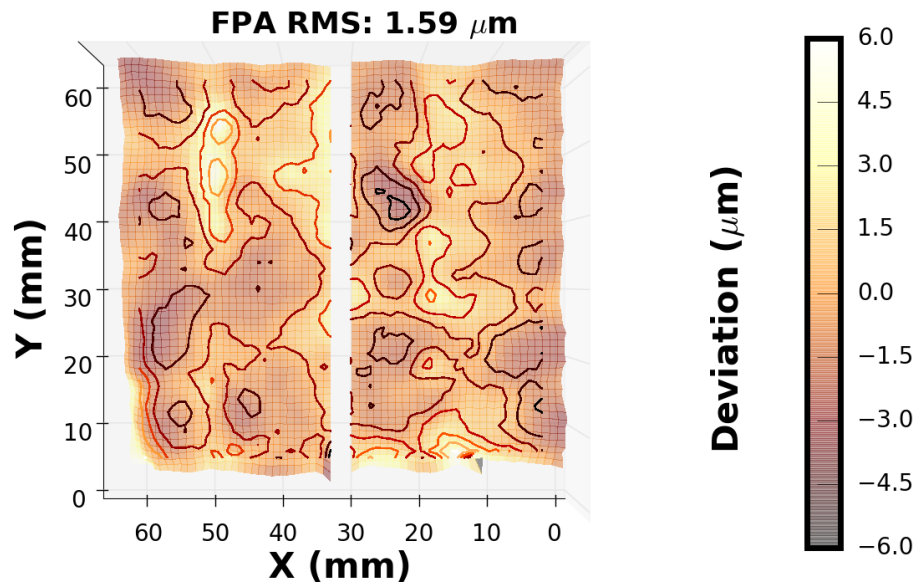


Figure 5. Contour map of the blue detector pair at room temperature; the changes going cold are negligible.

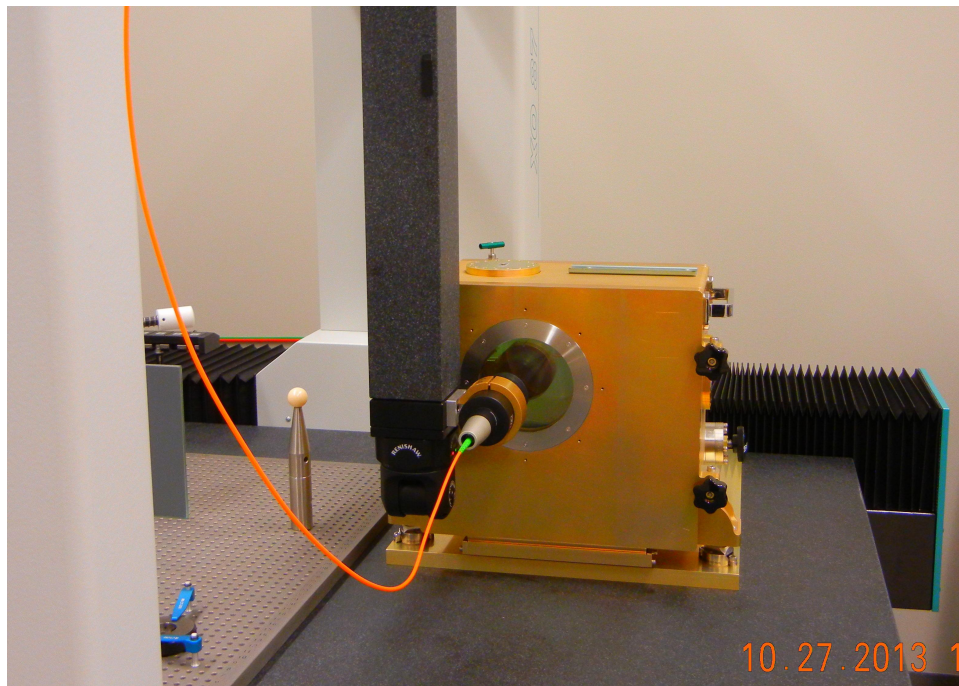


Figure 6. Photograph of the test cryostat mounted on the CMM table with the confocal microscope, set up to measure detector flatness.

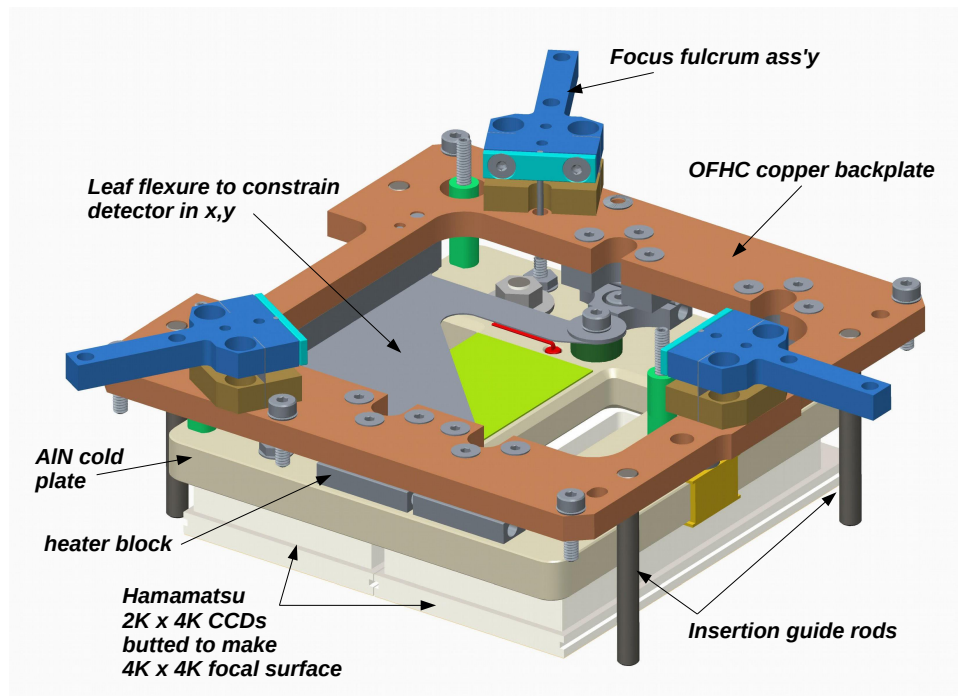


Figure 7. Cross-section of the CCD focal plane assembly looking from above. The preamp circuitry is suppressed.

A custom reflectometer can also be attached to the CMM arm which is fed by a fiber from the monochromator. It has reference and measuring diodes, and can provide reflectivity measurements for the detectors to compare with the actual QE measurements. The reflectance measurements are calibrated with a silicon standard, and the CMM is used both to accurately explore the reflectance over the surface of the detector and to explore the sensitivity to focus; in practice, the device is peaked up in the focus direction on both the standard and detector to ensure identical illumination geometry.

#### 4. THE CCD FOCAL PLANE ASSEMBLY

The CCD focal plane is illustrated in Figures 7 and 8. The assembly shown is mounted into an OFHC copper box suspended from the camera mechanical assembly in the cryostat.<sup>6</sup> A highly aspheric silica field lens is mounted immediately in front of the detector, with a vertex spacing of 1.5mm from the detector surface. The lens is thermally closely coupled to the copper mounting box, so the detector is effectively surrounded by cold. Three G10 arms (not shown) are mounted on the focus fulcrum assemblies shown and reach to linear screw actuators with vacuum stepper motors near the outside wall of the cryostat. The focus fulcrum assemblies attach to the coldplate through the focus rods and move the aluminum nitride coldplate mounting the CCDs by  $\pm 100$  microns for focus in response to the linear actuators at the ends of the arm moving about 8 mm. The lateral positioning of the detector is provided by the stainless steel leaf flexure shown.

The coldplate is thermally connected to the copper box via short 3-mil silver straps. The temperature of the detectors is maintained by a PID loop operating small heater resistors mounted in the the heater blocks shown. In operation, the cryocooler head will be maintained at a temperature which would in the absence of heat input at the detector result in a detector temperature about 2-3 degrees below the desired operating point. This set point is determined secularly by the average required power of the detector heaters and is changed only slowly. There is a small Klixon bimetal thermostatic switch on the coldplate to prevent overheating, though the maximum power into the detector heaters is only 2W, and overheating would not occur in ordinary circumstances even if the heater were left on at full power at room temperature.

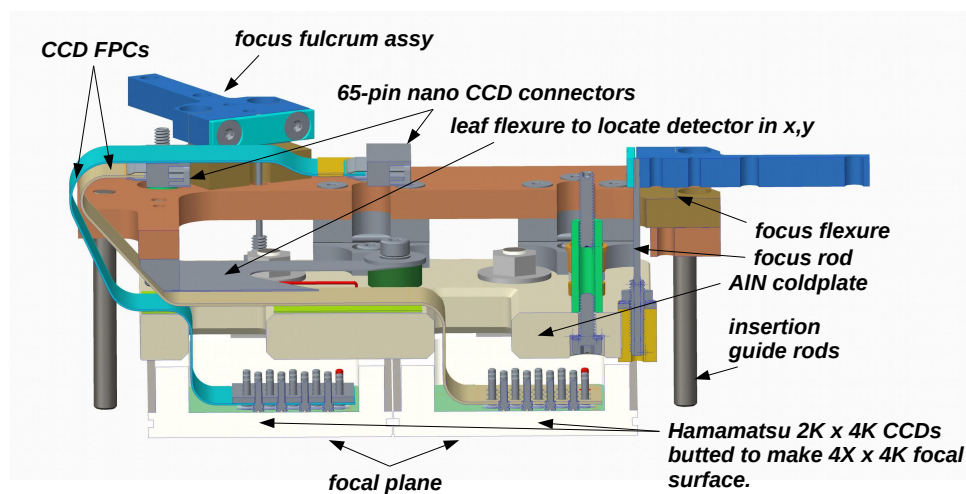


Figure 8. Cross-section of the CCD focal plane assembly from the side, showing the run of the FPCs from the detectors to the preamp.

The CCD clocks are brought in and analog video out from the detectors via custom 59-pin peelaway connectors incorporated into the FPCs to the preamp. The preamp is mounted just above the assembly shown and has mating connectors to the two 65-pin nanos on the FPCs. The clock signals are brought in to and the amplified video out of the preamp on a bundle of wires which run down one of the G10 focus arms and thence to the FEE/ADC board on a vacuum port near the focus mechanism at the end of the arm. The signal timing for the CCD is carefully designed so that nothing is happening in the digital realm during the critical CDS sampling, and the eight channels of analog video is delivered to the ADC board using twisted pairs.

## 5. PERFORMANCE OF THE CCD SYSTEM

The system has been tested with a pair of engineering-grade red CCDs, during which a few noise and reliability issues were addressed, and with the first pair of science-grade red chips after the design was finalized and final boards were made, populated, and tested.

The system displays excellent noise, linearity, and CTE performance from these preliminary tests. There is still some concern about dark current, though the impact of the currently measured dark current is slight.

The performance of the first red pair of CCDs is summarized in the table below. The first four amplifiers belong to CCD 1, the second to CCD 2. The noise level in the low-level CTE numbers is about .000012, which results in some measurements in excess of unity.

The measured dark current in the two devices is 5.6 and 5.2 electrons/hr at 158K, which is somewhat above the manufacturer's maximum spec at 173K. We discuss this discrepancy and its impact below.

amp	rdnoise	gain	rdnoise	1200e- CTE		100e- CTE	
	ADU	e-/ADU	e-	serial	parallel	serial	parallel
0	3.02	1.24	3.61	0.9999956	0.9999790*	0.9999966	0.9999608
1	3.03	1.24	3.78	0.9999964	0.9999848*	0.9999788	0.9999427
2	2.94	1.27	3.18	0.9999968	0.9999860	0.9999812	0.9999421
3	2.99	1.18	2.95	0.9999963	0.9999905	0.9999908	0.9999458
4	2.88	1.26	3.19	0.9999977	0.9999978	1.0000020	0.9999874
5	3.20	1.20	3.80	0.9999974	0.9999982	0.9999838	0.9999907
6	3.50	1.24	4.51*	0.9999986	0.9999978	1.0000136	0.9999873
7	2.93	1.26	3.18	0.9999987	0.9999981	1.0000047	0.9999914

The CTE performance is excellent, and remains so at low signal levels characteristic of the sky continuum in the red arm, about 100 electrons. The CTE numbers in this table were all measured using the charge residual method in the overscan region. We will overscan by about 64 pixels vertically and probably the same horizontally in each amplifier segment.

Note that with our inverse gain of about 1.3 electrons/ADU we do not reach physical full well when we saturate the ADC, so we cannot measure full well with this setup, nor do we really care what it is so long as it well exceeds our digital limit. This choice was made to better sample the noise histogram at the very low signals which we will typically have in the spectra. We do not expect to exceed our digital range with our typical 1000 second exposures with even the strongest night sky lines, and we will not observe sources bright enough to cause trouble.

These very thick devices, of course, have serious trouble with cosmic rays; an image showing the two adjacent upper corners of the red assembly is shown in Figure 9.

A plot showing linearity of the device at high signal levels is shown in Figure 10. Low-level linearity (not shown) is excellent, with no detectable deviations at levels as low as 10 ADU. The fact that the deviation is nonzero at zero signal in the figure is an artifact of the fitting, which was not constrained to go through zero at zero signal, but the low-level data shows that the linear response does, in fact, go to zero at zero signal to an accuracy of better than one electron.

A quite remarkable feature of the linearity is the uniformity of the error across the eight amplifiers. The amplifiers are represented by the colors, and the tight similarity is apparent; the amplifiers on the two devices are not more different than the small spread among the amplifiers on a single device. The nonlinearity itself, displayed this way, peaks in fractional amplitude at about -0.6% at about 10,000 ADU (13,000 electrons), tapers off, and rises to about +0.12% at about 30,000ADU, where it remains to about 55,000 ADU, and then falls to about -0.09% at digital full well. Note, however, that this description of the phenomenon is appropriate to the global fit used to fit the signal in the lower plot. The ‘nonlinearity’ between 0 and 10,000 ADU is simply a gain error of about 1.2%. If the gain is changed to accommodate this, the nonlinearity at levels below 10,000 ADU is essentially unmeasurable. The real nonlinearity at higher levels becomes, of course, much larger, and exhibits the usual positive signature due to the higher gain of the output FET at larger source-drain voltage, then the flattening at yet higher video levels. If the nonlinearity is described this way, the peak is at about 30,000 ADU and is about 1.4%; it remains at about this value to about 45000 ADU and then falls to about 1.2% at digital full well.

The astronomical signals expected in PFS are much smaller than 10,000 ADU, but understanding calibration and dealing with the strong OH night sky lines demands that we understand the nonlinearity well. Its extremely uniform behavior in the Hamamatsu devices will greatly facilitate this.

The measured dark current at -115C is about 5 electrons/hour, which is at the quoted limit from the manufacturer at -100C, and is much higher than the roughly 2 electrons/hour seen in a typical HSC device at this temperature. We are somewhat puzzled by this, but earlier data with the same pair shows even higher dark current, and we strongly suspect that we are seeing not real dark current but decaying fluorescence in the AIN

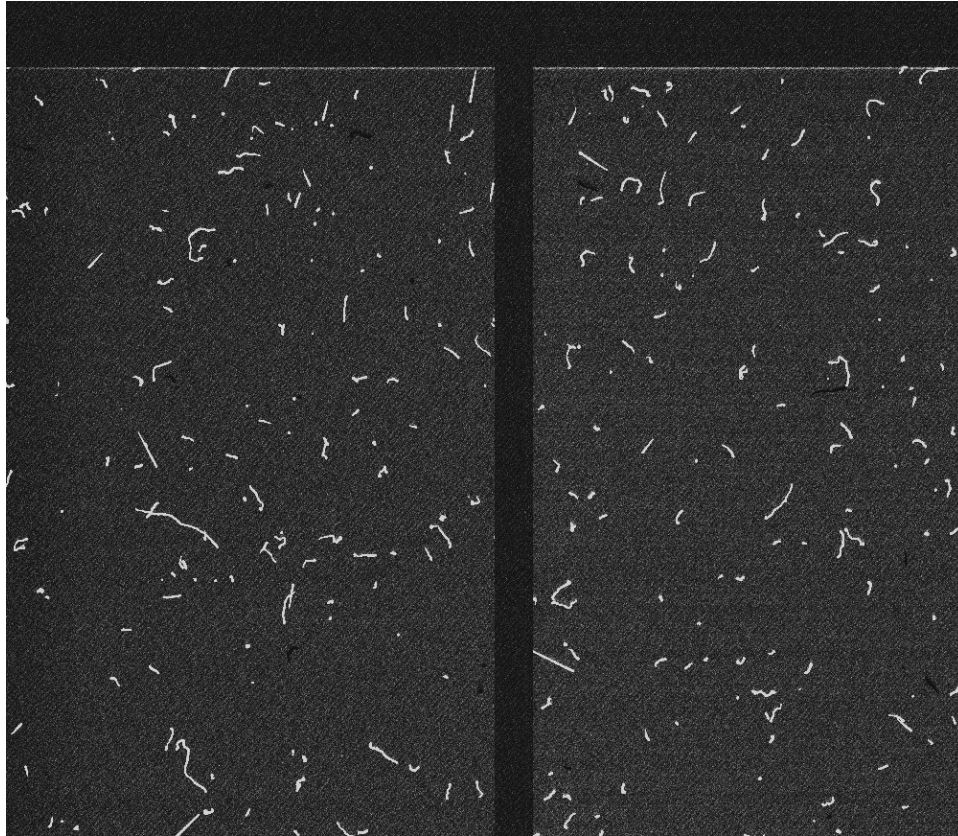


Figure 9. Expanded view of a 1200s dark frame showing the upper right corner of one CCD and the upper left corner of the other in the red focal plane assembly. The straight cosmic ray tracks are mostly muons; the erratically curved ones electrons.

substrates on the CCDs and the AlN coldplate. We will investigate the phenomenon in detail in tests on subsequent detectors; the tests on this first one were done while hardware and test procedures were being finalized and we were pressed by a shipping deadline, so were somewhat chaotic. At 5 electrons/hour, however, the dark noise affects final signal-t0-noise almost negligibly; the exposure times to reach a given S/N in cases in which the sky noise completely dominates are increased by only about half a percent.

In tests on subsequent detectors, we will measure QE at operating temperature, use the Fe55 source for independent measurement of gain and CTE, and employ the new subpixel illuminator to quantify pixel-to-pixel crosstalk, pixel response nonuniformity (if any), and the level dependence of these phenomena.

All in all, the Hamamatsu detectors appear to be an excellent choice for PFS, and perform extremely well at the very low light levels expected for our faint-object spectra.

## 6. THE NEAR IR SYSTEM

The optomechanics for the IR camera are in the final stages of design and early stages of fabrication. The camera is described in a paper presented in the 2014 SPIE conference<sup>9</sup> and has changed little since that publication. The mirror cell, detector support, and (now) the detector mounting box are all constructed of silicon carbide in a bonded assembly. The focal plane assembly is broadly similar to the CCD one, with the same focus mechanism and leaf flexure to support the H4RG detector, but the preamp is replaced by Teledyne's standard ground-based SIDECAR ASIC, which is mounted behind the detector in its shadow just as the preamp is for the CCDs. A cross-section of the focal plane assembly is shown in Figure 11

A custom FPC connects the SIDECAR to a SIDECAR Acquisition Module (SAM) mounted just outside the vacuum port servicing these signals. Again, a PC card is used for the vacuum feedthrough, though this one is

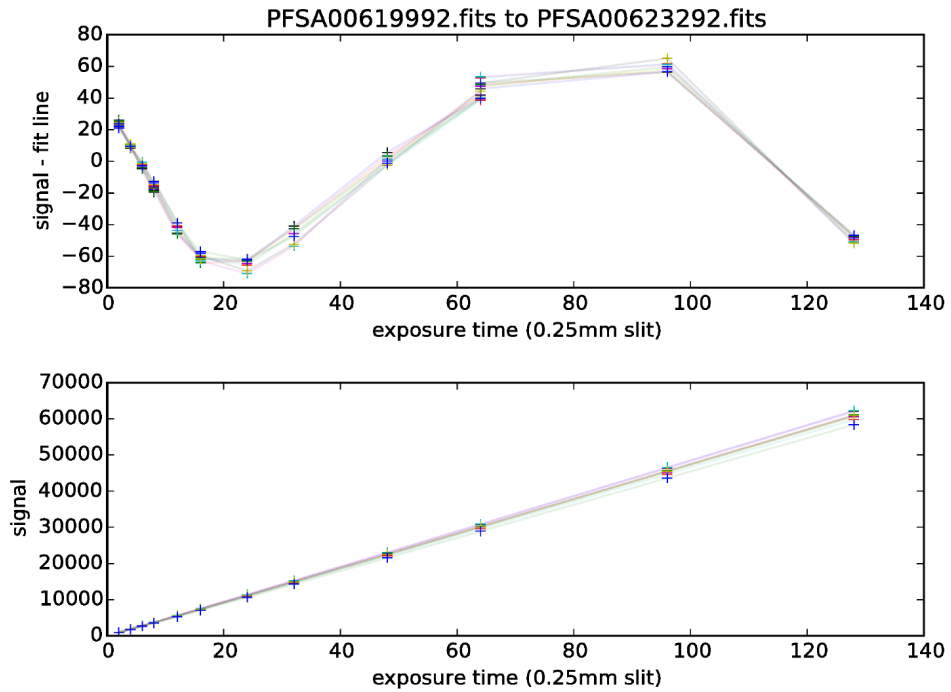


Figure 10. Nonlinearity of the red CCDs at high exposure levels. The deviations shown are from an unconstrained best-fit line over the whole range; set text for discussion.

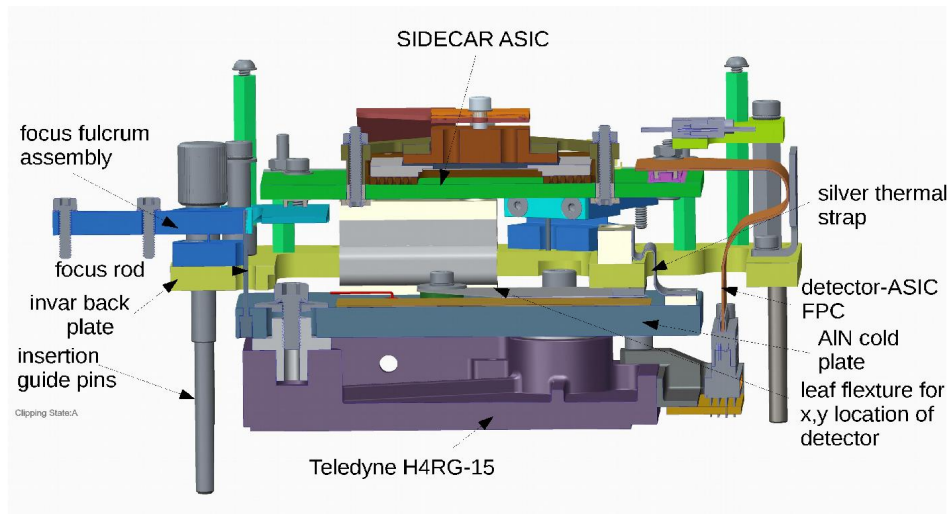


Figure 11. Cross-section of the IR focal plane assembly.

much simpler than the FEE/ADC board for the CCDs; it has only traces and a connector for the FPC on the vacuum part and a connector for the SAM on its edge.

After much work on a Linux software system to read HxRG detectors, at first aimed at a system using the gigabit ethernet port on the SAM, we have finally succeeded in producing such a system. There were, it turned out, essentially insurmountable problems (insufficient on-board memory) with the ethernet hardware for devices as large as the H4RG, and we have fallen back to a Linux implementation of the USB2.0 protocol, which has demonstrated itself to be very robust. This requires a processor reasonably close to the SAM, but the BEE PC104 processor is used for only trivial housekeeping tasks on the IR cryostat and should be capable of ingesting the incoming USB data from the SAM, 32 16-bit channels at 100kHz, and relaying that data over GigE to the observatory system. If that fails, much more powerful processors are available with the same or smaller physical footprint and similar or lower power consumption.

The modifications to the test cryostat to allow testing the H4RG are almost finished, and we will mount an engineering grade device in the cryostat for testing this summer, followed by a science-grade detector. We have in hand two science-grade devices from the first lot from our contract with Teledyne and one engineering-grade device. The first IR cryostat is scheduled for shipment next spring, the first blue one this summer. The first red one is already in France and is being tested. This complement of cryostats will furnish the first of the four spectrographs for the PFS system.

## ACKNOWLEDGMENTS

We gratefully acknowledge support from the Funding Program for World-Leading Innovative R&D in Science and Technology (FIRST), program: "Subaru Measurements of Images and Redshifts (SuMIRe)", CSTP, Japan, and support from JSPS KAKENHI Grant Numbers 15H05893, 15K21733, 15H05892.

## REFERENCES

- [1] Kamata, Y., Miyazaki, S., Nakaya, H., Komiyama, Y., Obuchi, Y., Kawanomoto, S., Uruguchi, F., Utsumi, Y., Suzuki, H., Miyazaki, Y., and Muramatsu, M., "Hyper Suprime-Cam: characteristics of 116 fully depleted back-illuminated CCDs," in [*High Energy, Optical, and Infrared Detectors for Astronomy V*], *Proc. SPIE* **8453**, 84531X (July 2012).
- [2] Sugai, H., Tamura, N., Karoji, H., Shimono, A., Takato, N., Kimura, M., Ohyama, Y., Ueda, A., Aghazarian, H., de Arruda, M. V., Barkhouser, R. H., Bennett, C. L., Bickerton, S., Bozier, A., Braun, D. F., Bui, K., Capocasale, C. M., Carr, M. A., Castilho, B., Chang, Y.-C., Chen, H.-Y., Chou, R. C. Y., Dawson, O. R., Dekany, R. G., Ek, E. M., Ellis, R. S., English, R. J., Ferrand, D., Ferreira, D., Fisher, C. D., Golebiowski, M., Gunn, J. E., Hart, M., Heckman, T. M., Ho, P. T. P., Hope, S., Hovland, L. E., Hsu, S.-F., Hu, Y.-S., Huang, P. J., Jaquet, M., Karr, J. E., Kempenaar, J. G., King, M. E., Fèvre, O. L., Mignant, D. L., Ling, H.-H., Loomis, C., Lupton, R. H., Madec, F., Mao, P., Marrara, L. S., Ménard, B., Morantz, C., Murayama, H., Murray, G. J., de Oliveira, A. C., de Oliveira, C. M., de Oliveira, L. S., Orndorff, J. D., de Paiva Vilaça, R., Partos, E. J., Pascal, S., Pegot-Ogier, T., Reiley, D. J., Riddle, R., Santos, L., dos Santos, J. B., Schwochert, M. A., Seiffert, M. D., Smeed, S. A., Smith, R. M., Steinkraus, R. E., Sodr e, L., Spergel, D. N., Surace, C., Tresse, L., Vidal, C., Vives, S., Wang, S.-Y., Wen, C.-Y., Wu, A. C., Wyse, R., and Yan, C.-H., "Prime Focus Spectrograph for the Subaru telescope: massively multiplexed optical and near-infrared fiber spectrograph," *Journal of Astronomical Telescopes, Instruments, and Systems* **1**, 035001 (July 2015).
- [3] Takada, M., Ellis, R. S., Chiba, M., Greene, J. E., Aihara, H., Arimoto, N., Bundy, K., Cohen, J., Dor e, O., Graves, G., Gunn, J. E., Heckman, T., Hirata, C. M., Ho, P., Kneib, J.-P., Fèvre, O. L., Lin, L., More, S., Murayama, H., Nagao, T., Ouchi, M., Seiffert, M., Silverman, J. D., Sodr e, L., Spergel, D. N., Strauss, M. A., Sugai, H., Suto, Y., Takami, H., and Wyse, R., "Extragalactic science, cosmology, and Galactic archaeology with the Subaru Prime Focus Spectrograph," *PASJ* **66**, R1 (Feb. 2014).
- [4] Fisher, C., Morantz, C., Braun, D., Seiffert, M., Aghazarian, H., Partos, E., King, M., Hovland, L. E., Schwochert, M., Kaluzny, J., Capocasale, C., Houck, A., Gross, J., Reiley, D., Mao, P., Riddle, R., Bui, K., Henderson, D., Haran, T., Culhane, R., Piazza, D., and Walkama, E., "Developing engineering model Cobra fiber positioners for the Subaru Telescope's prime focus spectrometer," in [*Advances in Optical and Mechanical Technologies for Telescopes and Instrumentation*], *Proc. SPIE* **9151**, 91511Y (July 2014).

- [5] de Oliveira, A. C., de Oliveira, L. S., de Arruda, M. V., Souza Marrara, L., dos Santos, L. H., Ferreira, D., dos Santos, J. B., Rosa, J. A., Junior, O. V., Pereira, J. M., Castilho, B., Gneiding, C., Junior, L. S., de Oliveira, C. M., Gunn, J., Ueda, A., Takato, N., Shimono, A., Sugai, H., Karoji, H., Kimura, M., Tamura, N., Wang, S.-Y., Murray, G., Le Mignant, D., Madec, F., Jaquet, M., Vives, S., Fisher, C., Braun, D., Schwochert, M., and Reiley, D. J., “Fiber optical cable and connector system (FOCCoS) for PFS/ Subaru,” in [*Advances in Optical and Mechanical Technologies for Telescopes and Instrumentation*], *Proc. SPIE* **9151**, 91514G (July 2014).
- [6] Vives, S., Le Mignant, D., Gunn, J. E., Smee, S., Souza de Oliveira, L., Tamura, N., Sugai, H., Barkhouser, R., Bozier, A., Carr, M. A., de Oliveira, A. C., Ferrand, D., Golebiowski, M., Hart, M., Hope, S., Jaquet, M., Madec, F., Pascal, S., Pegot-Ogier, T., and Vital de Arruda, M., “Current status of the spectrograph system for the SuMIRe/PFS,” in [*Ground-based and Airborne Instrumentation for Astronomy V*], *Proc. SPIE* **9147**, 914762 (July 2014).
- [7] Pascal, S., Vives, S., Barkhouser, R., and Gunn, J. E., “Optical design of the SuMIRe/PFS spectrograph,” in [*Ground-based and Airborne Instrumentation for Astronomy V*], *Proc. SPIE* **9147**, 914747 (July 2014).
- [8] Smee, S. A., Gunn, J. E., Golebiowski, M., Hope, S. C., Madec, F., Gabriel, J.-F., Loomis, C., Le fur, A., Dohlen, K., Le Mignant, D., Barkhouser, R., Carr, M. A., Hart, M., Tamura, N., Shimono, A., and Takato, N., “Visible camera cryostat design and performance for the SuMIRe Prime Focus Spectrograph (PFS),” in [*Ground-based and Airborne Instrumentation for Astronomy VI*], *Proc. SPIE* **9908** (July 2016).
- [9] Smee, S. A., Gunn, J. E., Golebiowski, M., Barkhouser, R., Vivès, S., Pascal, S., Carr, M., Hope, S. C., Loomis, C., Hart, M., Sugai, H., Tamura, N., and Shimono, A., “The near infrared camera for the Subaru Prime Focus Spectrograph,” in [*Ground-based and Airborne Instrumentation for Astronomy V*], *Proc. SPIE* **9147**, 91472V (Aug. 2014).
- [10] Hope, S. C., Gunn, J. E., Loomis, C. P., Fitzgerald, R. E., and Peacock, G. O., “CCD readout electronics for the Subaru Prime Focus Spectrograph,” in [*High Energy, Optical, and Infrared Detectors for Astronomy VI*], *Proc. SPIE* **9154**, 91542G (July 2014).
- [11] Hart, M., Barkhouser, R. H., Carr, M., Golebiowski, M., Gunn, J. E., Hope, S. C., and Smee, S. A., “Focal plane alignment and detector characterization for the Subaru prime focus spectrograph,” in [*High Energy, Optical, and Infrared Detectors for Astronomy VI*], *Proc. SPIE* **9154**, 91540V (July 2014).